# Multiwavelength fluorescence lidar observations of smoke plumes

Igor Veselovskii[1], Nikita Kasianik[1], Mikhail Korenskii[1], Qiaoyun Hu[2], Philippe Goloub[2], Thierry Podvin[2], Dong Liu[3]

[1] *Prokhorov General Physics Institute of the Russian Academy of Sciences, Moscow, Russia.*

[2] *Univ. Lille, CNRS, UMR 8518 - LOA - Laboratoire d'Optique Atmosphérique, F-59650 Lille, France*

[3] *State Key Laboratory of Modern Optical Instrumentation, College of Optical Science and Engineering: International Research Center for Advanced Photonics, Zhejiang University, Hangzhou 310027, China*

## Abstract

A five-channel fluorescence lidar was developed for the study of atmospheric aerosol. The fluorescence spectrum induced by 355 nm laser emission is analyzed in five spectral intervals using interference filters. Central wavelengths and the widths of these five interference filters are respectively: 438/29, 472/32, 513/29, 560/40 and 614/54 nm. The relative calibration of these channels has been performed using a tungsten-halogen lamp with color temperature 2800K. This new lidar system was operated during Summer – Autumn 2022, when strong forest fires occurred in the Moscow region and generated a series of smoke plumes analyzed in this study. Our results demonstrate that, for urban aerosol, the maximal fluorescence backscattering is observed in 472 nm channel. For the smoke the maximum is shifted toward longer wavelengths, and the fluorescence backscattering coefficients in 472 nm, 513 nm and 560 nm channels have comparable value. Thus, from the analysis of the ratios of fluorescence backscattering in available channels, we show that it is possible to identify smoke layers. The particle classification based on single channel fluorescence capacity (ratio of the fluorescence backscattering to elastic one), has limitations at high relative humidity (RH). The fluorescence capacity is indeed decreasing when water uptake of particles enhances the elastic scattering. However, the spectral variation of fluorescence backscattering does not exhibit any dependence on RH and can be therefore applied for aerosol identification.

## 1. Introduction

The knowledge of the chemical composition of atmospheric aerosol is important for characterization of its impact on the Earth radiation balance (Boucher et al., 2013; IPCC 2022).

The composition of aerosol, however, is strongly variable, and in practice, several general aerosol types are considered usually based on their origin (Dubovik et al., 2002). The Mie-Raman and high spectral resolution lidars provide the opportunity to derive vertical distribution of the particle extinction and backscattering coefficients together with multispectral depolarization ratio. The main aerosol types can be distinguished based on such observations (Burton et al., 2012, 2013; Groß et al., 2013; Mamouri et al., 2017; Papagiannopoulos et al., 2018; Nicolae et al., 2018; Hara et al., 2018; Wang et al., 2021; Mylonaki et al., 2021). However, due to the variability of the aerosol parameters, the particle intensive properties (properties that are independent of concentration), such as lidar ratios, depolarization ratios and Angstrom exponents can vary in a wide range, even for aerosols from the same origin, which complicates their identification.

The fluorescence measurements provide new independent information about aerosol composition, which can be used for classification. (Veselovskii et al., 2022b). Being induced by 355 nm laser radiation the atmospheric fluorescence emission spreads in a wide spectral range from approximately 380 nm to beyond 700 nm. The multianode photomultipliers combined with spectrometer, in principle, allow the profiling of the full fluorescence spectrum (Sugimoto et al., 2012; Saito et al., 2022; Reichardt et al., 2022). In a more simple approach a single fluorescence channel has been integrated into existing multiwavelength Mie-Raman lidar (Veselovskii et al., 2020), and a fraction of the fluorescence spectrum is selected by a wideband interference filter. High transmittance of modern interference filters (above 95%), allows efficient detection of fluorescence emission, and when combined with simultaneous depolarization measurements the main aerosol types, such as dust, smoke, pollen and urban aerosols can be identified (Veselovskii et al., 2022b). This classification scheme relies on the fluorescence capacity $G_\lambda$, which is the ratio of fluorescence backscattering to elastic backscattering at laser wavelength. The fluorescence capacity, however, depends on the relative humidity (RH), because enhanced elastic backscattering leads to decrease of $G_\lambda$ (Veselovskii et al., 2021). As a result, at high RH, we cannot discern unambiguously whether the decrease of $G_\lambda$ comes from water uptake or from changes in the aerosol composition.

The water uptake increases the elastic backscattering but normally does not alter the chemical components and consequently the total amount of fluorescent molecules within a particle does not change. The illumination intensity distribution within a particle, as well as the emission angular distribution can be altered by the change of particle size and refractive index during the hygroscopic growth. However, this effect occurs for relatively big microspheres with size parameter exceeding approximately 10 (Veselovskii et al., 2002). Thus, fluorescence of the fine mode particles should be less influenced by the hygroscopic growth. Our existing lidar data-base in well mixed boundary layer situations demonstrate that, at least, for urban and smoke particles, the fluorescence backscattering coefficient did not change during water uptake. Thus, we have good reason to expect, that fluorescence spectrum is not modified by the aerosol hygroscopic growth, and several fluorescence channels should provide more reliable information upon aerosol type.

Smoke is one of the most abundant aerosol types and it was intensively studied with Mie-Raman lidars for decades (Adam et al., 2020 and references therein). Smoke is characterized also by high fluorescence capacity (probably due to the presence of the organic carbon fraction), thus fluorescence lidar measurements proved to be very efficient for smoke identification and analysis (Hu et al., 2022, Veselovskii et al., 2022a,b). However, as mentioned, at high RH levels, the classification of smoke, based on a single channel fluorescence may fail. The solution could be the detection of fluorescence at several wavelengths. In July 2022 a new lidar system equipped with five fluorescence channels, was assembled in Prokhorov General Physics Institute, Troitsk, Moscow. The lidar was in operation during Summer and Autumn 2022, when strong forest fires occurred in the Moscow region. In this paper we analyze the spectral dependence of the fluorescence backscattering inside and outside the smoke plumes. The results demonstrate that the hygroscopic growth does not affect the spectral dependence of fluorescence backscattering.

## 2. Experimental setup

The fluorescence lidar is based on a tripled Nd:YAG laser with pulse energy of 80 mJ at 355 nm and repetition rate of 20 Hz. Backscattered light is collected by a 40 cm aperture Newtonian telescope and the lidar signals are digitized with Licel transient recorders with 7.5 m range resolution, allowing simultaneous detection in the analog and photon counting modes. The optical scheme of the receiving module is presented in Fig.1. The system is designed to detect elastic backscattering at 355 nm, nitrogen Raman backscattering at 387 nm and fluorescence backscattering in five spectral intervals. These intervals are separated with dichroic beamsplitters and isolated by the interference filters manufactured by Alluxa. The central wavelengths and the widths of transmission bands (FWHM) of these fluorescence channels are respectively: 438/29, 472/32, 513/29, 560/40 and 614/54 nm. The transmission of the filters exceeds 97%, while suppression of optical signal out of band is above OD6. To improve the suppression of elastic backscattering we installed two filters in tandem in every channel.

Laser radiation at 532 nm can induce additional aerosol fluorescence which will contaminate long-wave channels. To remove this potential contamination, the emissions at 532 nm and 1064 nm are separated with dichroic mirrors and redirected to an optical dump. Therefore, the laser beam sent into the atmosphere has only one wavelength - 355 nm. As follows from Fig.1, the 532 nm radiation is out of the transmission band of the filters, which prevents the leaking of residual 532 nm component to the fluorescence channels. We should mention, that the vibrational overtone of $N_2$ Raman scattering at 424.4 nm is within the transmission band of 438 nm channel. In accordance with results of Knippers et al. (1985), Raman intensity of this overtone is about three orders lower than intensity of $N_2$ fundamental vibration (for 488 nm laser wavelength). Based on our measurements, contribution of $N_2$ overtone to fluorescence signal from urban aerosol (with backscattering coefficient of 1.0 $Mm^{-1}sr^{-1}$ at 355 nm and $G_{438}$=0.3×$10^{-4}$) is estimated to be below 5% at 1000 m height. In all the channels the PMTs R9880U-01 were used, except in the 614 nm channel, where R9880-20 PMT was installed, due to its higher sensitivity in the red spectral region. The strong sunlight background at daytime restricts the fluorescence observations to only nighttime. All the observations presented in this study were performed at 45 degree angle to horizon.

The aerosol extinction coefficient at 355 nm ($\alpha_{355}$) was calculated from Raman observations as described in Ansmann et al., (1992). For the calculation of the backscattering coefficient $\beta_{355}$ in the presence of clouds, we used approach described in Veselovskii et al. (2022b). Additional information about atmospheric properties was available from radiosonde measurements at Dolgoprudnyi station, located about 50 km away from the observation site. It should be mentioned that the current lidar configuration does not allow measurement of the depolarization ratio.

The fluorescence backscattering coefficient $\beta_{F\lambda}$ is calculated from the ratio of fluorescence signal to 387 nm nitrogen Raman signal with correction for differential Raleigh and aerosol extinction, as described in Veselovskii et al. (2020). The atmospheric transmission of fluorescence signal is calculated for the wavelengths corresponding to the center of the filter transmission band. The error due to the neglect of spectral dependence of the Raleigh extinction inside the filter transmission band is the largest for the shortwave channel (438 nm). Computations show that at height of 4000 m corresponding error of $\beta_{F438}$ is below 4%. For correction of errors provided by the aerosol differential extinction we need to make an assumption about the value of the extinction Angstrom exponent (EAE). In particular, for the aged smoke the EAE for 355/532 nm wavelengths is about 1.0 (Hu et al., 2022) and this value was used in the data analysis in our study. The uncertainties, due to possible deviation of EAE from 1.0 value are analyzed in section 3.1 of this paper.

For calculation of $\beta_{F\lambda}$ one needs to know the differential cross section of nitrogen Raman scattering, $\sigma_R$, and the relative sensitivity of the nitrogen and fluorescence detection channels. The value $\sigma_R$=2.744*$10^{-30}$ $cm^2sr^{-1}$ at 355 nm was taken from Venable et al. (2011). Sensitivity of R9880U-01 photocathode in the 387 nm - 438 nm range varies for less than 10%, so we neglect this variation and calculate relative sensitivity of the PMTs as described in Veselovskii et al. (2020). The relative sensitivity of the rest of the fluorescence channels in respect to the 438 nm one, was calculated from laboratory measurements using a tungsten-halogen lamp Thorlabs QTH10/M with color temperature 2800K as a source, assuming this source follows the Planck blackbody emission. For calibration, the telescope is installed horizontally and the lamp is placed at a distance of 4 m from the entrance. The screen, installed in front of the telescope, selected the central part of the lamp radiation of 50 mm diameter, which was used for calibration. This procedure was performed once a week and variations of the calibration coefficients during August-September 2022 period were below 15% for the 614 nm channel and below 10% for the rest of the channels. Thus, the uncertainties of $\beta_{F\lambda}$ calculation include the systematical errors of calibration procedure ($\varepsilon_{cal}$), the errors due to indeterminacy of the choice of the Angstrom exponent ($\varepsilon_A$), and the statistical errors of the measurements ($\varepsilon_{st}$). For the vertical profiles of the fluorescence backscattering in section 3, we do not provide the systematical errors of the calibration, however, $\varepsilon_{cal}$ are considered, when the spectra of the fluorescence backscattering are analyzed.

One should note that $\beta_{F\lambda}$ is the integral of fluorescence backscattering over the filter transmission band $D_\lambda$. To compare $\beta_{F\lambda}$ at different fluorescence channels we compute the mean backscattering coefficients per elementary spectral interval, $B_\lambda = \frac{\beta_{F\lambda}}{D_\lambda}$, denoted as “fluorescence spectral backscattering coefficient”. The fluorescence capacity $G_\lambda$, which is the ratio of the fluorescence backscattering to the elastic one, in principle, can be calculated for any laser wavelength. In our previous studies we calculated $G_\lambda$ with respect to $\beta_{532}$, however, in this work, it was calculated with respect to 355 nm $G_\lambda = \frac{\beta_{F\lambda}}{\beta_{355}}$, since 532 nm wavelength was not available. All $\beta_{F\lambda}$, $G_\lambda$ and $B_\lambda$ profiles presented in this work were smoothed with the Savitzky – Golay method, using a second order polynomial with 7 points in the window.

## 3. Measurements and analysis

In August 2022 numerous smoke layers originating from the forest fires in Ryazan region (about 160 km South – East of Moscow) were detcted over the lidar station. The travel time of the layers was less than two days, thus smoke can be considered as fresh. The previous fluorescence studies of smoke plumes transported over Atlantic and including 466/44 nm fluorescence measurements revealed that fluorescence capacity (calculated for $\beta_{532}$), in the absence of hygroscopic growth, varied within the range (2.5–5.0)$\times 10^{-4}$ (Veselovskii et al., 2021, 2022a,b; Hu et al., 2022). The Backscattering Angstrom Exponent (BAE) of smoke for 355/532 nm wavelengths, is about 2.0, and fluorescence capacity $G_{472}$ in 472/32 nm channel (calculated for $\beta_{355}$ from past studies) is expected to be in the range (0.8–1.6)$\times 10^{-4}$. Here and below the fluorescence capacity will be provided for 472 nm, because in most of the cases the fluorescence in this channel was maximal.

### 3.1. Fluorescence measurements during smoke episode

***27-28 August 2022***

Two-day backward trajectories from the NOAA HYSPLIT model for the air mass reaching Moscow on 28 August at 00:00 UTC are shown in Fig.2. Air masses observed at 1500 m, passed over the fire region, close to the ground, and should thus contain biomass burning aerosols. The relative humidity measured by the radiosonde, at 00:00 UTC, was about 35% at 1000 m and increased with height up to 70% at 3000 m. Temporal evolution of the aerosol backscattering coefficient, $\beta_{355}$, fluorescence backscattering, $\beta_{F472}$, and fluorescence capacity, $G_{472}$, are shown in Fig.3. Aerosols are localized mainly below 3000 m, while above 4000 m cloud layers can be seen. The highest fluorescence backscattering values were encountered before 20:30 UTC inside the boundary layer. The fluorescence capacity exceeds $2.5\times10^{-4}$, which is the highest $G_{472}$ observed in our measurements. After 20:30 $G_{472}$ decreases but remains above $1.0\times10^{-4}$, which, in principle, can be due to mixing of smoke with urban aerosol.

Vertical profiles of the fluorescence spectral backscattering coefficients $B_\lambda$ are shown in Fig.4a for the period that exhibited the highest fluorescence capacity (19:00-20:00 UTC). The profiles of $B_{472}$, $B_{513}$, $B_{560}$ are similar, and the ratios $B_{472}/B_{513}$, $B_{472}/B_{560}$ in Fig.4b are close to 1.0.. The fluorescence capacity $G_{472}$ is above $2.0\times10^{-4}$, in 1.0 km – 2.5 km height range, where $\beta_{355}$ and $B_\lambda$ are maximal. To quantify the uncertainty due to indeterminacy of the EAE choice, the Fig.4c shows profiles of $B_{472}$, $B_{614}$ and the ratios $B_{472}/B_{513}$, $B_{472}/B_{614}$ calculated for values of EAE $A$=0.5, 1.0, 1.5. The optical depth at 355 nm exceeded 0.55 at 3000 m height. The aerosol differential extinction provides the largest effect to $B_{614}$, and the difference between values obtained with $A$=1.0 and 1.5 at 3000 m is about 6.5%. For $B_{472}$ this difference is lower, about 5%. However, for the ratios of fluorescence backscattering, the influence of aerosol is lower: for both $B_{472}/B_{513}$ and $B_{472}/B_{614}$ corresponding difference is below 2.0%.

Fluorescence spectra of two distinct temporal intervals can be seen in Fig.5. In the interval corresponding to high fluorescence capacity (19:00-20:00 UTC), the maximum fluorescence backscattering is observed in 513 nm channel, which agrees with the spectrum of smoke fluorescence provided by Reichard et al. (2022). In the second interval (23:00-01:00 UTC), when fluorescence capacity is lower, the fluorescence is maximal at 472 nm and at longer wavelengths it decreases fast. The lidar ratios ($S_{355}$) for both time intervals are shown in the same figure. For the first interval (with maximum $G_{472}$) $S_{355}$ is about 60 sr, while for the second interval $S_{355}$ decreases to about 40 sr. The highest spectral fluorescence capacity of smoke (capacity per elementary spectral interval), reported by Reichard et al. (2022) for 455–535 nm range is about $8\times10^{-6}$ nm$^{-1}$. This is very comparable with our value ($11\times10^{-6}$ nm$^{-1}$) calculated from data plotted in Fig.4 and 5 at 472 nm in the 19:00-20:00 UTC time interval.

The variation of the fluorescence spectra is revealed by the ratio of the fluorescence backscattering coefficients at different wavelengths (e.g. $B_{472}/B_\lambda$). In particular, inside the aerosol plume in Fig.3 $B_\lambda$ does not change significantly in 472 – 560 nm range, and the ratios $B_{472}/B_{513}$, $B_{472}/B_{560}$ are close to 1.0. Spatio-temporal evolution of these ratios is shown in the right column in Fig.3. The intervals with the maximum $G_{472}$ are well distinguished by minimum $B_{472}/B_{513}$ and $B_{472}/B_{560}$ ratios. At the same time, ratio $B_{472}/B_{438}$ appears to be less sensitive to $G_{472}$ changes.

Actually, this ratio even increases inside the aerosol plume. Thus, the analysis of Fig.3 reveals two types of the particles. The first type having a high fluorescence capacity ($G_{472}$>2.0×10$^{-4}$) and a lidar ratio close to 60 sr can be classified as “pure” smoke. The second type, with lower fluorescence capacity ($G_{472}$~1×10$^{-4}$) and a smaller lidar ratio, can be a mixture of smoke and urban aerosol.

Forest fires stopped in the beginning of September, so during September – October the urban aerosols were predominant. Fig.6 shows corresponding fluorescence spectra, normalized to $B_{472}$. Measurements were performed during 07:00-09:00 UTC and averaged within the boundary layer between 500 m and 1000 m. For urban aerosols, fluorescence at wavelengths larger than 472 nm decreases fast. Presence of remaining smoke, however, may lead to some increase of $B_\lambda$ in the 513 – 614 nm interval. For urban aerosol particles the fluorescence capacity $G_{472}$ for urban particles varied within (0.1-0.4)×10$^{-4}$ and the lidar ratios within 30-50 sr interval. Thus, mixing of smoke and urban particles can explain the variability observed in fluorescence spectrum on Fig.5.

***17 August 2022***

The spatio – temporal intervals with high fluorescence capacity were observed also for other days. On August 17-18, 2022 between 18:00 – 19:00 UTC, fluorescence capacity at 472 nm, the $G_{472}$, within the aerosol plume increased above 1.0×10$^{-4}$ (Fig.7). Simultaneously, the ratio $B_{472}/B_{560}$ decreases to less than 0.8. Outside the plume, the fluorescence capacity is (0.4-0.7)×10$^{-4}$ and the ratio $B_{472}/B_{560}$ increases up to 1.2. Corresponding fluorescence spectra are shown in Fig.8. Inside the plume the fluorescence is maximal in the 560 nm channel, while outside the maximum is shifted to 472 nm. Similarly to the 27-28 August event (Fig.5), the lidar ratio $S_{355}$ is about 60 sr inside the plume and decreases down to about 30 sr outside the plume. Thus, again, we conclude that in the interval having the highest $G_{472}$, smoke particles are predominant, while outside we very likely addressed a mixture of smoke and urban aerosol.

### 3.2. Analysis of fluorescence profiles observed in the presence of hygroscopic growth of aerosol.

Our previous studies with a single channel fluorescence lidar revealed, that the hygroscopic growth of aerosol particles decreases the fluorescence capacity, but does not affect the fluorescence backscattering coefficient (Veselovskii et all, 2021). Thus, when fluorescence spectra are available, one can expect that spectral dependence of fluorescence backscattering coefficients will preserve information about particle type (will not be influenced by water uptake). Below, we provide interpretation of the measurements performed during the nights August 21-22 and 23-24 2022. In both cases, RH increased with altitude and the hygroscopic growth is one possible contributor to the observed increase of particle backscattering coefficient. Our results show, that on August 21-22 the shape of the fluorescence spectrum (the set of $B_\lambda/B_{472}$ ratios) did not exhibit any change with altitude, whereas, conversely, on August 23-24 the shape of the fluorescence spectrum has changed with altitude, indicating possible change of aerosol composition with height.

Fig.9. shows vertical profiles of the fluorescence spectral backscattering coefficients, $B_{\lambda,}$ together with backscattering $\beta_{355}$ coefficient, fluorescence capacity $G_{472}$, and $B_{472}/B_{438}$, $B_{472}/B_{513}$, $B_{472}/B_{560}$ ratios on August 21 2022. Profiles of $B_{472}/B_{614}$ ratio are noisier and not used for analysis. The profile of relative humidity measured by a radiosonde at Dolgoprudnyi station, shows increase of RH with altitude from 30% to 80% within 1000-4500 interval. Inside 3000-4000 m range, the fluorescence backscattering does not demonstrate significant variations while elastic backscattering increases by two orders of magnitude (from approximately 1 $Mm^{-1}sr^{-1}$ to 100 $Mm^{-1}sr^{-1}$), which should be attributed to aerosol hygroscopic growth. The fluorescence capacity, $G_{472}$, decreases to less than $0.01\times10^{-4}$ at 4000 m, however, the ratios $B_{472}/B_{438}$, $B_{472}/B_{513}$, $B_{472}/B_{560}$ do not change with altitude, meaning that i) the spectrum (its shape) is not affected by water uptake process and that ii) aerosol composition remains constant.

Temporal evolution of the particle parameters on the August 23-24 night is presented in Fig.10. The relative humidity increases with height and during 18:00-20:00 time interval a cloud was formed at ~3000 m. After 20:00 the fluorescence capacity inside 2000-3000 m height range is low (below $0.2\times10^{-4}$), however low values of $G_{472}$ can also be explained by particle hygroscopic growth, thus one can not yet conclude that aerosol composition has changed, because the two effects (RH + aerosol changes) can occur simultaneously. Meanwhile, $B_{472}/B_{560}$ ratio decreases above 2000 m, which can be an indication of aerosol composition change. Profiles of aerosol properties for the time interval 20:30-23:30 are shown in Fig.11. In accordance with the radiosonde measurements the relative humidity reaches 80% at 3000 m at 00:00 UTC. At 1000 m height, where RH is low (~35%), $G_{472}$ is about $0.4\times10^{-4}$, hence, urban aerosol type is predominant. Both $B_{472}/B_{513}$ and $B_{472}/B_{560}$ ratios decrease above 2000 m, while $B_{472}/B_{438}$ increases. As mentioned above, such behavior can be an indication that contribution of smoke rises with height.

Normalized fluorescence spectra for two height intervals, 1000-1500 m and 2500-3000 m are shown in Fig.11c. In the second interval, the spectrum is shifted towards longer wavelengths, which corroborates that smoke fraction in the aerosol mixture increases above 2000 m. Thus, the analysis of this episode demonstrates that multi-spectral fluorescence backscattering provides opportunity for particle identification even in the presence of hygroscopic growth.

## Conclusions and perspectives

Observations performed with a five-channel fluorescence lidar allow estimation of atmospheric aerosol fluorescence spectrum. For urban aerosol type the maximum of fluorescence is observed at 472 nm. However, for smoke particles, the maximum is shifted toward longer wavelengths and the fluorescence backscattering coefficients in the 472 nm, 513 nm and 560 nm channels are comparable. Hence, the ratios $B_{472}/B_{513}$ or $B_{472}/B_{560}$, allow identification of the smoke layers because, for smoke, these ratios are smaller than for urban particles.

During strong forest fires in August 2022 we regularly observed over Moscow aerosol plumes, characterized by high fluorescence capacity ($G_{472}$>1.0×10$^{-4}$). Inside these plumes, lidar ratio $S_{355}$ increased up to 60 sr simultaneously with a shift of the fluorescence maximum to 513 nm or 560 nm. Particles inside plume are very likely composed of “pure” smoke, while outside the plume, a smoke/urban mixture is probable. Classification of aerosol particles based on single channel fluorescence measurements has limitations at high RH because the fluorescence capacity is decreasing due to water uptake. However, our experimental database of fluorescence backscattering ratios does not show noticeable dependence with RH, which means these ratios allow us to identify smoke layers even in the presence of hygroscopic growth.

In our measurements, the laser emitted only 355 nm radiation. However, such configuration is not optimum for aerosol characterization: it is important to use dual-wavelength (355, 532 nm) depolarization and lidar ratio measurements together with the fluorescence observations. Such Laser Induced Fluorescence Exploratory instrument (LIFE) is currently under construction and will start operation in 2023, at LOA, ATOLL platform (France), in the frame of the OBS4CLIM project and AGORA-Lab research and development activities. More generally, it seems promising to upgrade widely-used multiwavelength Mie-Raman high performance lidars with a couple of fluorescence channels. According to our results, at least for smoke, the 472 nm and 513 nm channels can be considered. The wavelengths of aniti-Stokes components of nitrogen and oxygen stimulated by 532 nm radiation are 473 nm and 491 nm respectively. The oxygen component is blocked by the filter, while the nitrogen one is inside the transmission band of the 472 nm channel. The power of anti-Stokes scattering increases with temperature, but even at $30C^0$ its contribution to the fluorescence signal is insignificant. Estimations show that for backscattering coefficient $\beta_{355}$=1.0 $Mm^{-1}sr^{-1}$ and $\beta_{F513}=0.2\times10^{-4}$ $Mm^{-1}sr^{-1}$ (urban aerosol), the relative contribution of the nitrogen anti-Stokes component to the fluorescence (the fraction of $\beta_{F472}$) at 1000 m height is below $4\times10^{-4}$.

The results presented in this study are preliminary. We focused mainly on the fresh smoke analysis. However, smoke particle fluorescence properties depend on its chemical composition, in particular, on its organic carbon fraction. In addition, smoke fluorescence may be influenced by the burning process and transportation conditions. More observation campaigns, at different locations, are needed to clarify this. In the coming Spring – Summer period analysis of fluorescence spectra of different aerosol types, in particular, the pollens, is planned. At present, the system used in this study is being modified to include depolarization capability.

***Data availability***. Lidar measurements are available upon request (philippe.goloub@univ-lille.fr).

***Author contributions***. IV assembled the lidar and wrote the paper. NK and MK performed the measurements. QH, and PG analyzed data and helped with paper preparation. TP helped with lidar design, DL participated in paper preparation.

.

***Competing interests***. The authors declare that they have no conflict of interests.

**Acknowledgement**

Development of the lidar system was supported by Russian Science Foundation (project 21-17-00114). We acknowledge funding from the CaPPA project funded by the ANR through the PIA under contract ANR-11-LABX-0005-01, the “Hauts de France” Regional Council (project CLIMIBIO) and the European Regional Development Fund (FEDER). ESA/QA4EO program is greatly acknowledged for support of observation activity at LOA as well as OBS4CLIM Equipex project funded by ANR.

## References


Adam, M., Nicolae, D., Stachlewska, I. S., Papayannis, A., and Balis, D.: Biomass burning events measured by lidars in EARLINET – Part 1: Data analysis methodology, Atmos. Chem. Phys., 20, 13905–13927, https://doi.org/10.5194/acp-20-13905-2020, 2020.

Ansmann, A., Riebesell, M., Wandinger, U., Weitkamp, C., Voss, E., Lahmann, W., and Michaelis, W.: Combined Raman elastic-backscatter lidar for vertical profiling of moisture, aerosols extinction, backscatter, and lidar ratio, Appl.Phys.B, *55*, 18-28, 1992.

Boucher, O., Randall, D., Artaxo, P., Bretherton, C., Feingold, G., Forster, P., Kerminen, V.-M., Kondo, Y., Liao, H., Lohmann, U., Rasch, P., Satheesh, S. K., Sherwood, S., Stevens, B., and Zhang, X. Y.: Clouds and Aerosols, in: Climate Change 2013: The Physical Science Basis. Contribution of Working Group I to the Fifth Assessment Report of the Intergovernmental Panel on Climate Change, edited by: Stocker, T. F., Qin, D., Plattner, G.-K., Tignor, M., Allen, S. K., Boschung, J., Nauels, A., Xia, Y., Bex, V., and Midgley, P.,M., Cambridge University Press, Cambridge, United Kingdom and New York, NY, USA, 2013

Burton, S. P., Ferrare, R. A., Hostetler, C. A., Hair, J.W., Rogers, R. R., Obland, M. D., Butler, C. F., Cook, A. L., Harper, D. B., and Froyd, K. D.: Aerosol classification using airborne High Spectral Resolution Lidar measurements – methodology and examples, Atmos. Meas. Tech., 5, 73–98, 2012. https://doi.org/10.5194/amt-5-73-2012

Burton, S. P., Ferrare, R. A., Vaughan, M. A., Omar, A. H., Rogers, R. R., Hostetler, C. A., and Hair, J. W.: Aerosol classification from airborne HSRL and comparisons with the CALIPSO vertical feature mask, Atmos. Meas. Tech., 6, 1397–1412, 2013. https://doi.org/10.5194/amt-6-1397-2013

Dubovik, O., Holben, B. N., Eck, T. F., Smirnov, A., Kaufman, Y. J., King, M. D., Tanre, D., and Slutsker, I.: Variability of absorption and optical properties of key aerosol types observed in worldwide locations, J. Atmos. Sci., 59, 590–608, 2002.

Groß, S., Esselborn, M., Weinzierl, B., Wirth, M., Fix, A., and Petzold, A.: Aerosol classification by airborne high spectral resolution lidar observations, Atmos. Chem. Phys., 13, 2487–2505, 2013. https://doi.org/10.5194/acp-13-2487-2013

Hara, Y., Nishizawa, T., Sugimoto , N., Osada, K., Yumimoto, K., Uno, I., Kudo, R., and Ishimoto, H.: Retrieval of aerosol components using multi-wavelength Mie-Raman lidar and comparison with ground aerosol sampling, Remote Sens., 10, 937, 2018. https://doi:10.3390/rs10060937

Hu, Q., Goloub, P., Veselovskii, I., and Podvin, T.: The characterization of long-range transported North American biomass burning plumes: what can a multi-wavelength Mie-Raman-polarization-fluorescence lidar provide? Atmos. Chem. Phys. 22, 5399–5414, 2022 https://doi.org/10.5194/acp-22-5399-2022

Knippers,W., van Helvoort, K., and Stolte, S.: Vibrational overtones of the homonuclear diatomics (N2, O2, D2) observed by the spontaneous 385 Raman effect, Chem. Phys. Let., 121, 279–286, 1985. https://doi.org/10.1016/0009-2614(85)87179-7

Mamouri, R.-E., and Ansmann, A.: Potential of polarization/Raman lidar to separate fine dust, coarse dust, maritime, and anthropogenic aerosol profiles, Atmos. Meas. Tech., 10, 3403–3427, 2017. https://doi.org/10.5194/amt-10-3403-2017

Mylonaki, M., Giannakaki, E., Papayannis, A., Papanikolaou, C.-A., Komppula, M., Nicolae, D., Papagiannopoulos, N., Amodeo, A., Baars, H., and Soupiona, O.: Aerosol type classification analysis using EARLINET multiwavelength and depolarization lidar observations, Atmos. Chem. Phys., 21, 2211–2227, 2021. https://doi.org/10.5194/acp-21-2211-2021

Nicolae, D., Vasilescu, J., Talianu, C., Binietoglou, I., Nicolae, V., Andrei, S., and Antonescu, B.: A neural network aerosol-typing algorithm based on lidar data, Atmos. Chem. Phys., 18, 14511–14537, 2018. https://doi.org/10.5194/acp-18-14511-2018

Papagiannopoulos, N., Mona, L., Amodeo, A., D'Amico, G., Gumà Claramunt, P., Pappalardo, G., Alados-Arboledas, L., Guerrero- Rascado, J. L., Amiridis, V., Kokkalis, P., Apituley, A., Baars, H., Schwarz, A.,Wandinger, U., Binietoglou, I., Nicolae, D., Bortoli, D., Comerón, A., Rodríguez-Gómez, A., Sicard, M., Papayannis, A., and Wiegner, M.: An automatic observation-based aerosol typing method for EARLINET, Atmos. Chem. Phys., 18, 15879–15901, 2018. https://doi.org/10.5194/acp-18-15879-2018

Reichardt, J., Behrendt, O., and Lauermann, F.: Spectrometric fluorescence and Raman lidar: absolute calibration of aerosol fluorescence spectra and fluorescence correction of humidity measurements, Atmos. Meas. Tech., 16, 1–13, 2023. https://doi.org/10.5194/amt-16-1-2023

Saito,Y., Hosokawa, T., Shiraishi, K.: Collection of excitation-emission-matrix fluorescence of aerosol-candidate-substances and its application to fluorescence lidar monitoring, Appl. Opt., 61, 653 – 660, 2022.

Sugimoto, N., Huang, Z., Nishizawa, T., Matsui, I., Tatarov, B.: Fluorescence from atmospheric aerosols observed with a multichannel lidar spectrometer," Opt. Expr. 20, 20800-20807, 2012.

Venable, D. D., Whiteman, D. N., Calhoun, M. N., Dirisu, A.O., Connell, R. M., Landulfo, E.: Lamp mapping technique for independent determination of the water vapor mixing ratio calibration factor for a Raman lidar system, Appl. Opt., 50, 4622 - 4632, 2011.

Veselovskii, I., Griaznov, V., Kolgotin, A., Whiteman, D.: "Angle- and size-dependent characteristics of incoherent Raman and fluorescent scattering by microsoheres 2.: Numerical simulation", Appl. Opt. 41, 5783-5791, 2002

Veselovskii, I., Hu, Q., Goloub, P., Podvin, T., Korenskiy, M., Pujol, O., Dubovik, O., Lopatin, A.: Combined use of Mie-Raman and fluorescence lidar observations for improving aerosol characterization: feasibility experiment, Atm. Meas. Tech., 13, 6691–6701, 2020. doi.org/10.5194/amt-13-6691-2020.

Veselovskii, I., Hu, Q., Goloub, P., Podvin, T., Choël, M., Visez, N., and Korenskiy, M.: Mie–Raman–fluorescence lidar observations of aerosols during pollen season in the north of France, Atm. Meas. Tech., 14, 4773–4786, 2021. doi.org/10.5194/amt-14-4773-2021

Veselovskii, I., Hu, Q., Ansmann, A., Goloub, P., Podvin, T., Korenskiy, N.: Fluorescence lidar observations of wildfire smoke inside cirrus: A contribution to smoke-cirrus - interaction research, Atmos. Chem. Phys., 22, 5209–5221, 2022a. https://doi.org/10.5194/acp-22-5209-2022a.

Veselovskii, I., Hu, Q., Goloub, P., Podvin, T., Barchunov, B., and Korenskii, M.: Combining Mie–Raman and fluorescence observations: a step forward in aerosol classification with lidar technology, Atmos. Meas. Tech., 15, 4881–4900, 2022b. https://doi.org/10.5194/amt-15-4881-2022.

Wang, N., Shen, X., Xiao, D., Veselovskii, I., Zhao,C., Chen, F., Liu, C., Rong, Y., Ke, J., Wang, B., Qi, B., Liu, D.: Development of ZJU high-spectral-resolution lidar for aerosol and cloud: feature detection and classification, Journal of Quantitative Spectroscopy & Radiative Transfer, v.261, 107513, 2021. doi.org/10.1016/j.jqsrt.2021.107513

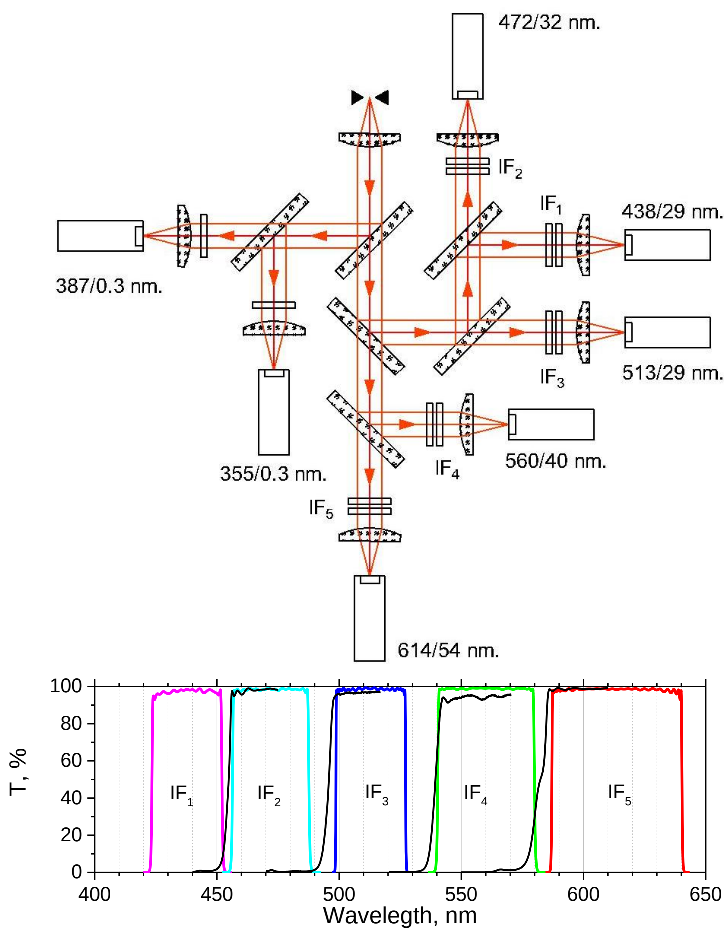


Fig.1. Optical scheme of the receiving module of the lidar together with transmissions of interference filters $IF_1$-$IF_5$ in the fluorescence channels. Black lines show the transmissions of the 45 degree dichroic beam splitters used for separation of fluorescence spectral components.

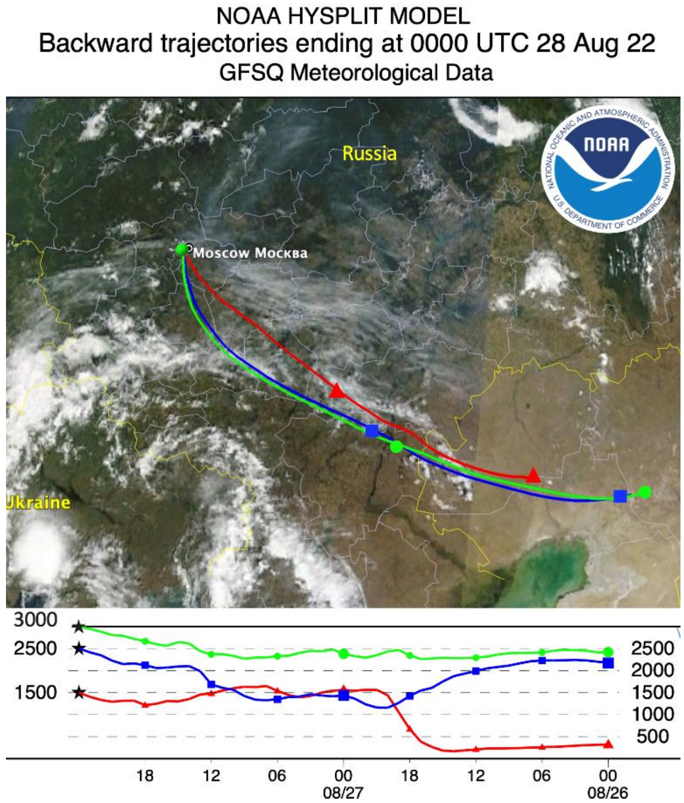


Fig.2. Two-day backward trajectories from the NOAA HYSPLIT model for the air mass in Moscow on 28 August at 00:00 UTC. The basemap is the Earth's true color image observed by MODIS Terra for the same period.

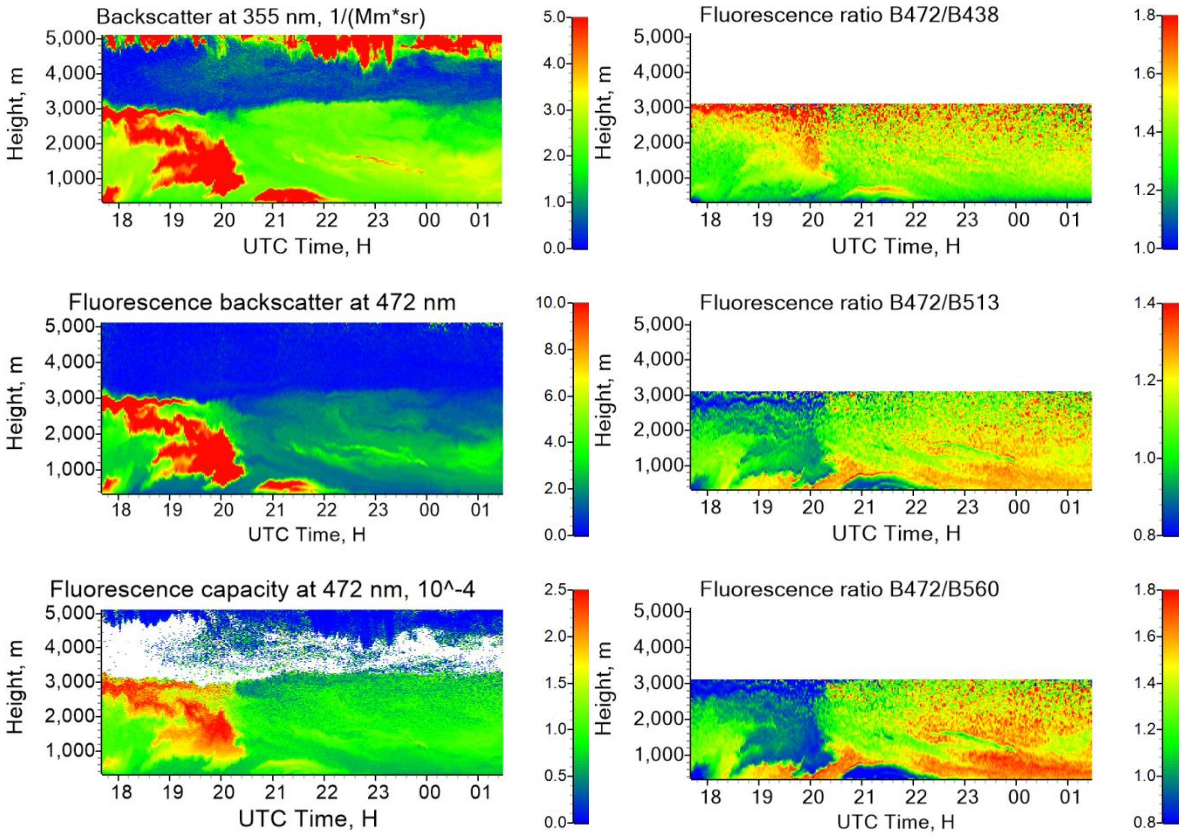


Fig.3. Spatio – temporal distribution of particle parameters on the night 27-28 August 2022. (left column) Aerosol backscattering coefficient $\beta_{355}$, fluorescence backscattering $\beta_{F472}$ (in $10^{-4}$ $Mm^{-1}sr^{-1}$), fluorescence capacity $G_{472}$. (right column) Ratios of fluorescence spectral backscattering coefficients $B_{472}/B_{438}$, $B_{472}/B_{513}$, $B_{472}/B_{560}$.

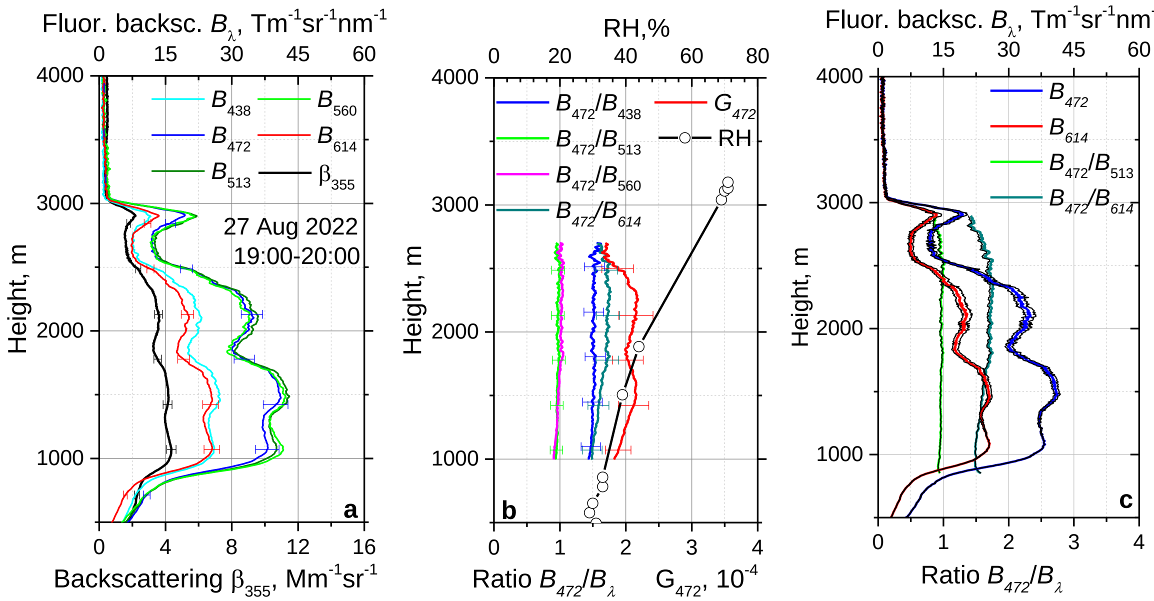


Fig.4. Observations on 27 August 2022 for period 19:00-20:00 UTC. (a) Fluorescence spectral backscattering coefficients $B_{\lambda}$ at 438, 472, 513, 560, 614 nm and the aerosol backscattering coefficient $\beta_{355}$. (b) The ratios $B_{472}/B_{438}$, $B_{472}/B_{513}$, $B_{472}/B_{560}$, $B_{472}/B_{614}$ and the fluorescence capacity $G_{472}$. Symbols show the relative humidity measured by a radiosonde at 00:00 UTC on 28 August. (c) Fluorescence spectral backscattering coefficients $B_{\lambda}$ at 472, 614 nm wavelengths and the ratios $B_{472}/B_{513}$, $B_{472}/B_{614}$ calculated for the Angstrom exponent values $A$=0.5, 1, 1.5. Results for $A$=0.5, 1.5 are shown with thin black lines, the increase of $A$ decreases the $B_{\lambda}$. The profiles at plots (a, b) are calculated for $A$=1.

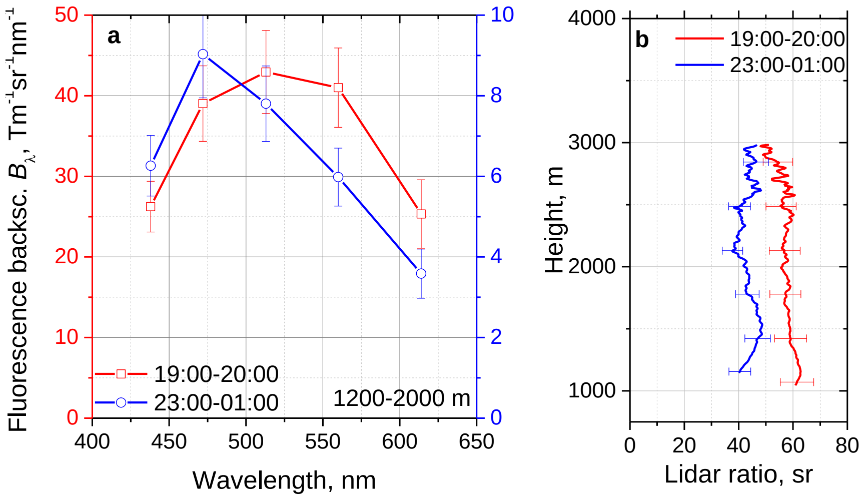


Fig.5. (a) Spectrum of fluorescence backscattering $B_\lambda$ on the night 27-28 August 2022 for 19:00-20:00 and 23:00-01:00 UTC intervals. Results are averaged inside 1200-2000 m height range. (b) Profiles of lidar ratios at 355 nm for the same temporal intervals.

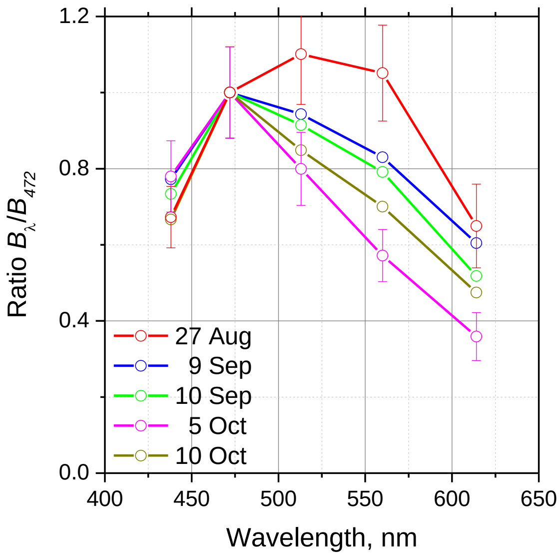


Fig.6. Fluorescence spectra measured in September - October 2022, when forest fires were over. Fluorescence backscattering coefficients $B_\lambda$ were averaged inside 500 – 1000 m height range and normalized on $B_{472}$. For comparison, the fluorescence spectrum in smoke plume on 27 August from Fig.5 is also presented.

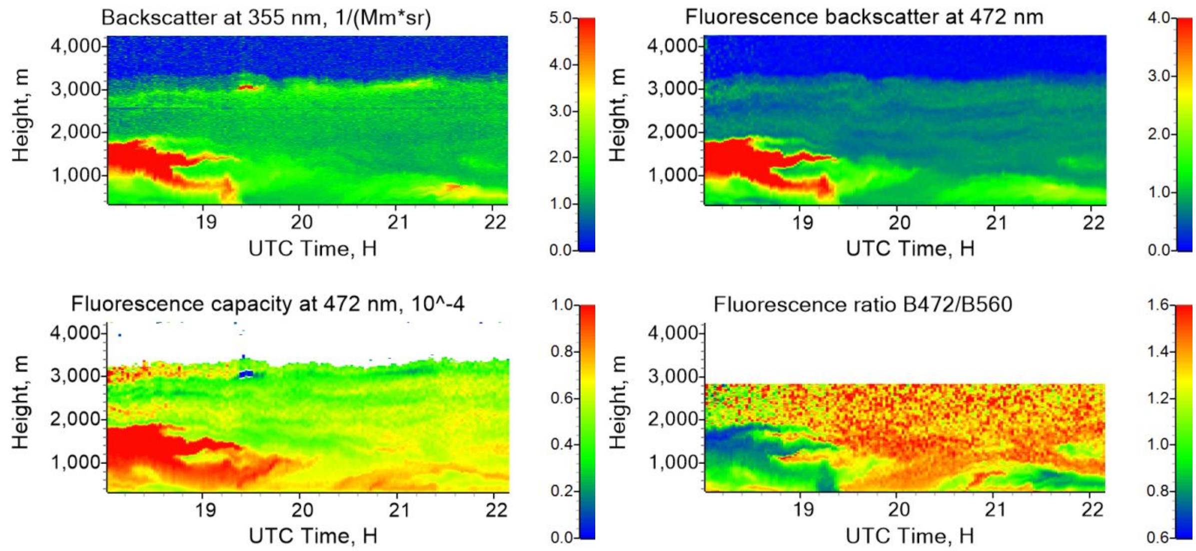


Fig.7. Observations on 17 August 2022. (left column) Aerosol backscattering coefficient $\beta_{355}$ and fluorescence capacity $G_{472}$. (right column) Fluorescence backscattering coefficient $\beta_{F472}$ (in $10^{-4}$ $Mm^{-1}sr^{-1}$) and the ratio of fluorescence spectral backscattering coefficients $B_{472}/B_{560}$.

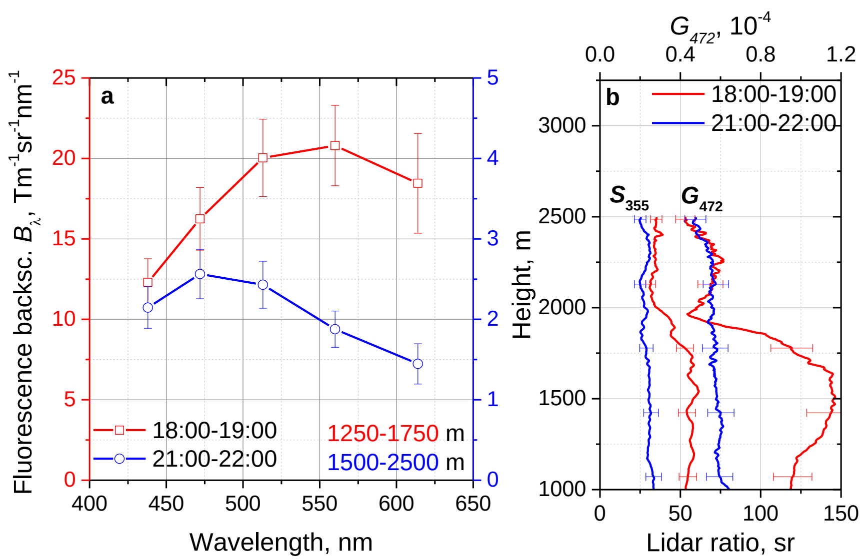


Fig.8. (a) Spectra of fluorescence backscattering $B_\lambda$ on 17 August 2022 for 18:00-19:00 UTC and 21:00-22:00 UTC periods. Results are averaged within 1250-1750 m and 1500-2500 m height ranges respectively. (b) Profiles of lidar ratio $S_{355}$ and fluorescence capacity $G_{472}$ for the same temporal periods.

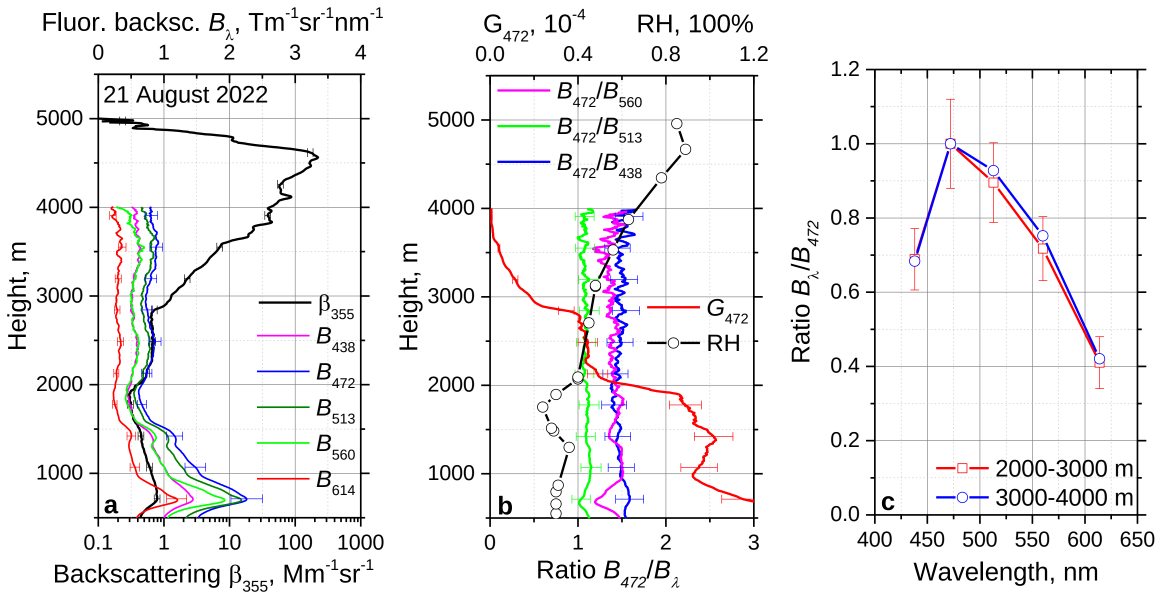


Fig.9. Vertical profiles of the particle parameters on 21 August 2022 for period 22:00-24:00 UTC. (a) The fluorescence spectral backscattering coefficients $B_\lambda$ at 438, 472, 513, 560, 614 nm and the aerosol backscattering coefficient $\beta_{355}$. (b) The ratios $B_{472}/B_{438}$, $B_{472}/B_{513}$, $B_{472}/B_{560}$ and the fluorescence capacity $G_{472}$. Symbols show the relative humidity measured by a radiosonde at 00:00 UTC on 22 August. (c) Spectrum of the fluorescence backscattering coefficient $B_\lambda$ for height intervals 2000-3000 m and 3000-4000 m. Values of $B_\lambda$ are normalized on $B_{472}$.

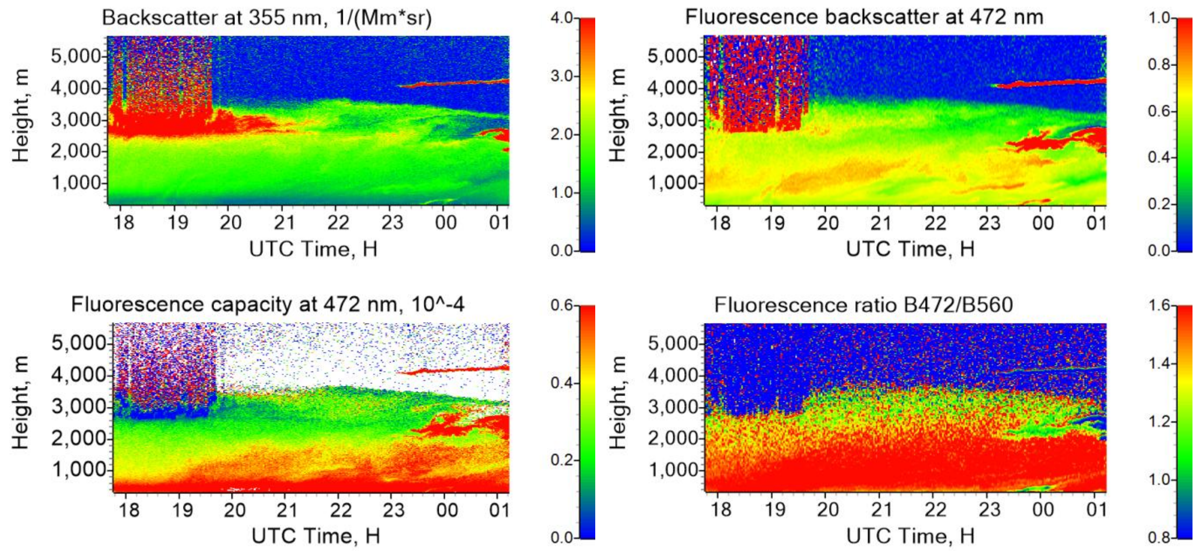


Fig.10. Spatio-temporal distributions of the particle parameters on the night 23-24 August 2022. (left column) The aerosol backscattering coefficient $\beta_{355}$ together with the fluorescence capacity $G_{472}$. (right column) The fluorescence backscattering coefficient $\beta_{F472}$ (in $10^{-4}$ $Mm^{-1}sr^{-1}$) and the ratio $B_{472}/B_{560}$.

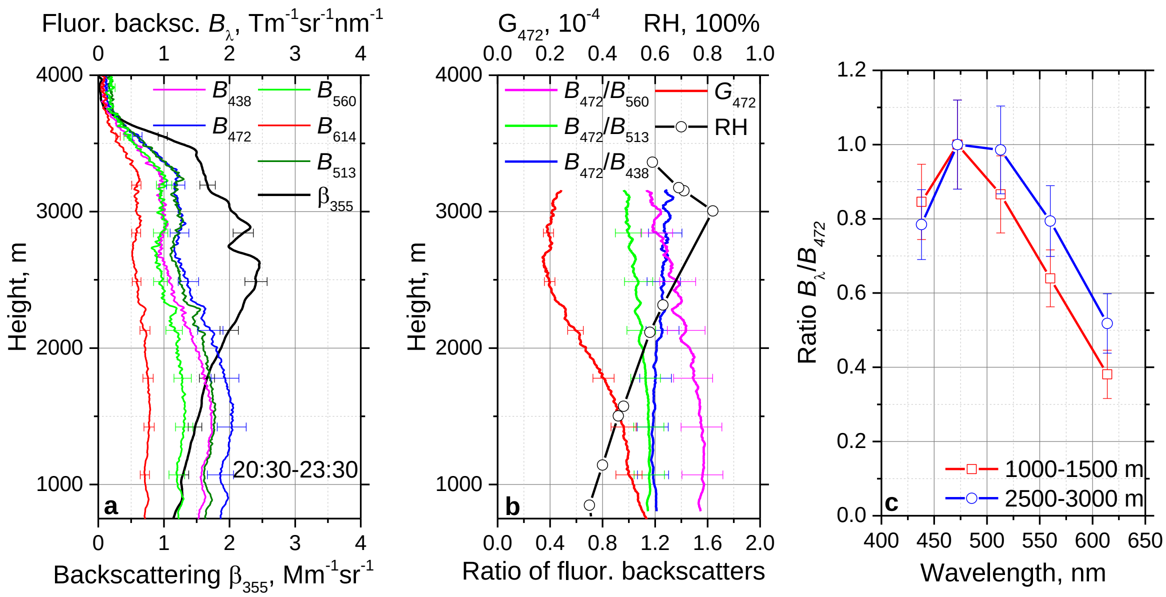


Fig.11. Vertical profiles of the particle parameters on 23 August 2022 for period 20:30-23:30 UTC. (a) The fluorescence spectral backscattering coefficients $B_\lambda$ at 438, 472, 513, 560, 614 nm and the aerosol backscattering coefficient $\beta_{355}$. (b) The ratios $B_{472}/B_{438}$, $B_{472}/B_{513}$, $B_{472}/B_{560}$ and the fluorescence capacity $G_{472}$. Symbols show the relative humidity measured by a radiosonde at 00:00 UTC on 24 August. (c) Spectrum of the fluorescence backscattering coefficient $B_\lambda$ for height intervals 1000-1500 m and 2500-3000 m. Values of $B_\lambda$ are normalized on $B_{472}$.